Supplementary information

A nanoparticle probe for the imaging of autophagic flux in live mice via magnetic resonance and near-infrared fluorescence

In the format provided by the authors and unedited

Contents:

1. Physical Properties and Activation of ADN

The physical properties of ADN and FH-Cy5.5 are extremely similar (Table S1), with the only notable difference being the presence/absence of arginine rich peptides linking the Cy5.5 moieties to FH.

Table S1. Physical properties of ADN and FH-Cy5.5

|	ADN	FH-Cy5.5
Autophagy detection	Yes	No
Poly Arg peptide	Yes	No
Valency (Cy5.5/NP)	4.8±0.7	4.9± 0.9
Cy5.5 fluorescence	Activatable	Always on
Size (nm)	21.8±0.4	16.3±1.3
Zeta potential (mV)	-9.3±0.7	-11.6±1.5
Blood $t_{1/2}$ (minutes)	50.7±3.4	65.8±0.6

We postulate that the arginine-rich peptides in ADN play a crucial role in facilitating fluorochrome-fluorochrome interactions, resulting in fluorochrome stacking and the quenching of unactivated ADN (see absorbance spectra in Figure 1 of main text). This is likely mediated by the propensity of arginine-rich peptides to self-aggregate due to energetically-favorable guanidinium side-chain stacking,[1] bringing the hydrophobic Cy5.5 fluorochromes on the surface of ADN into extremely close proximity with one another (Figure S1). Evidence for this mechanism is provided by i) the spectral shift of the Cy5.5 peak in the unactivated and activated forms of ADN, ii) the presence of this shift when ADN is placed in aqueous solution but not in methanol, and iii) the absence of a spectral shift in FH-Cy5.5 (see Figure 1 of main text).

A Quenched ADN   **B** Activated ADN   **C** FH-Cy5.5
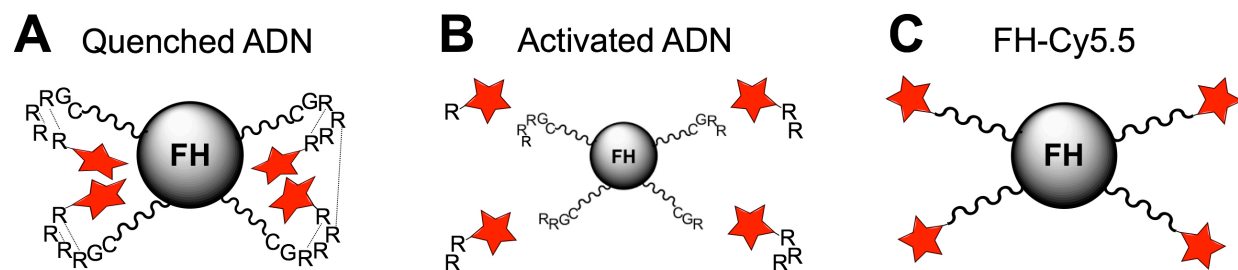
Figure S1. Postulated mechanism of fluorochrome quenching in unactivated ADN (Images are not drawn to scale for demonstration purposes). **A.** Self-aggregation of the polyarginine side chains (dashed lines) is energetically favorable and brings the Cy5.5 fluorochromes into extremely close proximity with one another. **B.** Cleavage of the peptide by cathepsins can occur at any of the arginine positions, and results in the separation of the fluorochromes and the loss of quenching. **C.** The distance between the fluorochromes in FH-Cy5.5 is sufficient to avoid fluorochrome-fluorochrome interactions and quenching.

## 2. Non Activatable D-Isomer of ADN

To further validate the activation mechanism of ADN, we synthesized a second control nanoparticle, FH-D-iso, in which the amino acids in the peptide were changed from an L to a D configuration (Figure S2). The L-isomer of the peptide can be cleaved by cathepsins and other proteases while the D-isomer cannot. The sequence of the peptide is R-R-R-R-G-C. Five of the six amino acids in the peptide could be changed to a D-configuration. Glycine, however, does not exist in a D-configuration and the D-peptide thus remained theoretically cleavable at that point. The properties of ADN and FH-D-iso, including charge and solubility, are otherwise identical. As shown in Figure 2 of the main text, a profound increase in fluorescence in starved cells was seen with ADN but not FH-D-iso. This confirms that the activation of ADN does indeed reflect its cleavage by lysosomal cathepsins.
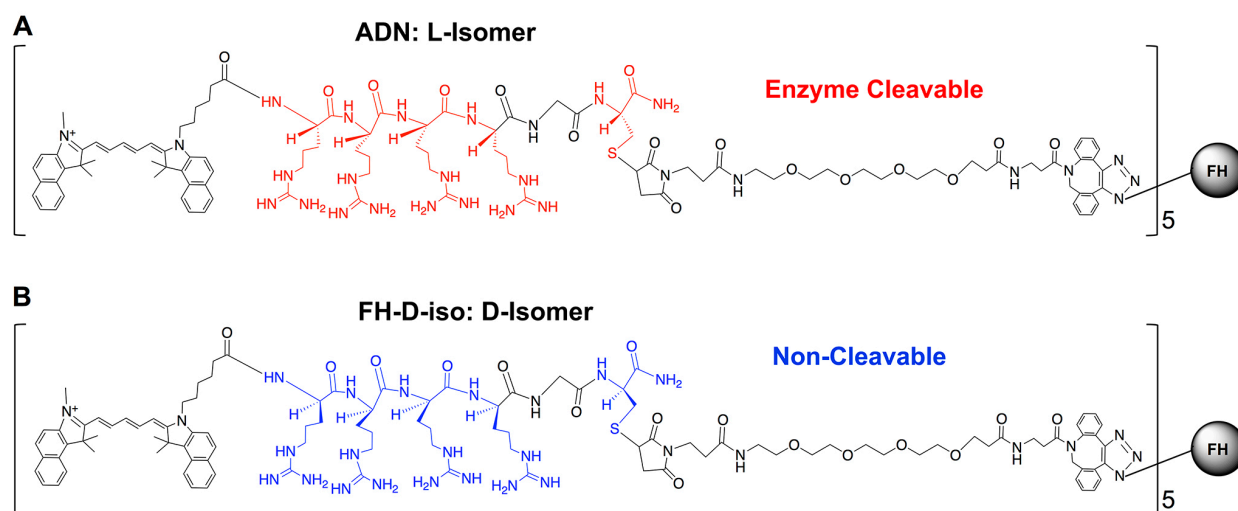
Figure S2. Schematic of ADN and the control nanoparticle FH-D-iso. A. The peptides in ADN exist in a cathepsin-cleavable L-configuration. **B.** In contrast, the amino acids in FH-D-iso (other than glycine) are arranged in D-configuration, which is resistant to cleavage by cathepsins/proteases. The chemical and physical properties of the activatable ADN and non-activatable FH-D-iso are otherwise identical.

3. Specificity of ADN using siRNA

The specificity of ADN for autophagy was further demonstrated using murine embryonic fibroblasts (MEFs) with genetic deletion of ATG5 or ATG7,[2] and in H9C2 cells with knockdown of ATG7 by siRNA (see Figure 2 of main text). Within 48 hours of siRNA exposure the level of ATG7 mRNA in H9C2 cells (rat cardiac myoblast cell line) had dropped to almost non-detectable levels (Figure S3). No effect on ATG7 was seen with the scrambled non-coding RNA (siNC). In starved H9C2 cells a significant increase in the ratio of LC3II/I was seen, suggestive of autophagy induction. The knockdown of ATG7 by siRNA completely eliminated this increase (Figure S3). The knockdown of ATG7 in H9C2s by siRNA was thus specific and efficient and, in conjunction with the ATG5-/- and ATG7-/- MEFS, provided a robust loss of function control with which to assess the specificity of ADN to detect autophagy.
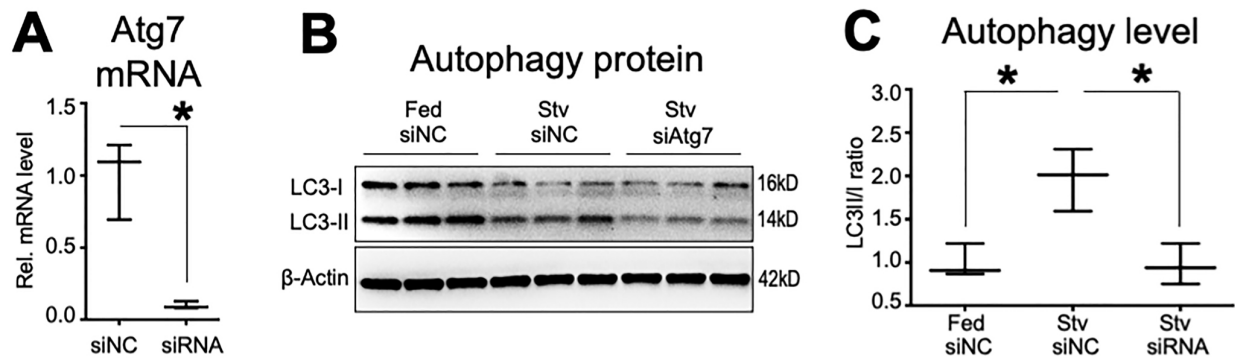
Figure S3. siRNA of ATG7 in H9C2 cells. A. mRNA levels of ATG7 are not affected by the non-coding control (siNC, n=3) but are significantly reduced by the siRNA to ATG7 (n=6, *p=0.0238 compared to siNC, by two-tailed Mann-Whitney test). Box plots show min, max and median. **B-C.** Western blot of LC3 in fed cells exposed to siNC, starved cells exposed to siNC, and starved cells exposed to siRNA to ATG7. The ratio of LC3II/I is elevated in starved cells exposed to siNC, but not in fed cells or starved cells with knockdown of ATG7. N=3 per group. *p=0.0110 (Fed siNC vs. Stv siNC), *p=0.01 (Stv siNC vs. Stv siRNA) by one-way ANOVA with Tukey post-test. Box pots show min, max and median. Uncropped gels are shown at the end of this Supplementary Information file.

4. Transmission electron microscopy of ADN in autophagosomes

Transmission electron microscopy (TEM) of starved H9C2 cells exposed to PBS (control) or ADN was performed to further demonstrate the uptake of ADN by early autophagosomes. The preparation, staining and imaging of the cells is described in the methods section of the main text. The starved H9C2 cells were exposed to PBS or ADN for 1 hour, replicating the conditions used in the ADN/LC3-GFP fluorescence co-localization experiments (main text, Figure 2L-M). In the starved H9C2 cells exposed to ADN multiple small electron-dense (dark) foci, characteristic of iron-oxide nanoparticles,[3,4] were routinely seen within the cell's autophagosomes (Figure S4). These electron-dense foci are produced by the iron-oxide core in ADN, which is 5-8 nm in size,[3,4] and further demonstrate that ADN is taken up by early autophagosomes. This pattern was not seen in the starved control cells exposed to PBS.
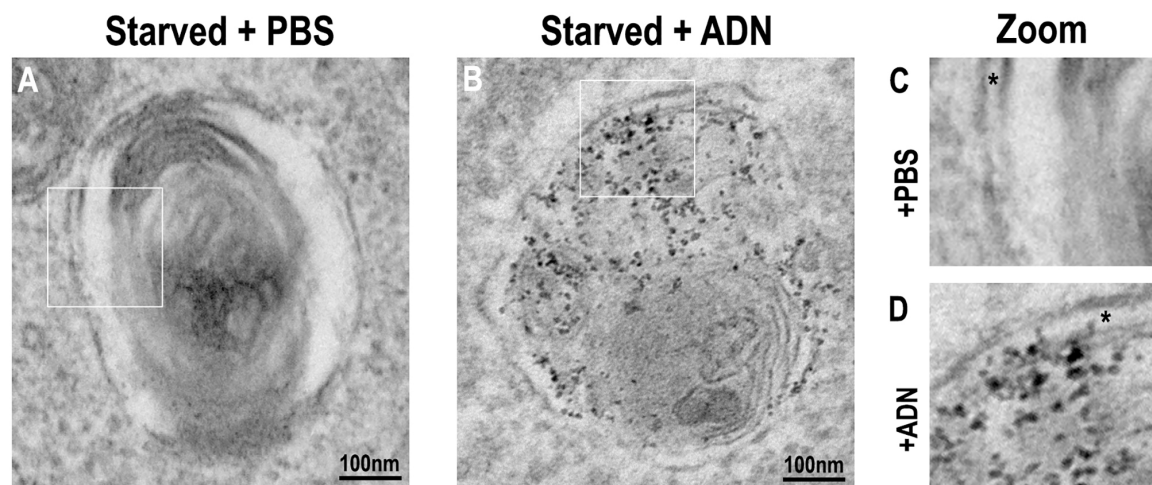
Figure S4: Transmission Electron Microscopy of ADN in Autophagosomes. Starved H9C2 cells were exposed to PBS (control) or ADN for 1 hour. **(A-B)** Autophagosomes in starved H9C2 cells exposed to **(A)** PBS or **(B)** ADN. (n=3 separate samples for each condition with consistent results). The characteristic double membrane of the autophagosomes, and the cytoplasmic organelles/contents within them, can be clearly seen. In the starved cells exposed to ADN **(B)** the probe, which produces small electron-dense foci from its iron-oxide core, was routinely internalized by autophagosomes. The white boxes show areas that have been magnified by 2x in panels C-D. **(C-D)** Magnified view of autophagosomes from cells exposed to **(C)** PBS or **(D)** ADN. The autophagosomes are enclosed by double membranes with a lucent space (asterisks) in between. In the cells exposed to ADN **(D)** small dark electron-dense foci, characteristic of iron-oxide nanoparticles, are highly visible within the interior of the autophagosome.

5. Detection by MRI: Insights from DX-1 surface staining of ADN

ADN can be detected in one of three ways: 1) Using the DX1 antibody to dextran,[5] which coats the surface of the FH moiety in ADN, 2) via cleavage of the arginine-rich peptides on the probe by lysosomal cathepsins, resulting in dequenching and the emission of Cy5.5 fluorescence, and 3) via a dramatic increase in the magnetic relaxivity of ADN when it is aggregated in autophagosomes/lysosomes and undergoes a magnetic relaxation switch effect.[6,7] In the absence of ADN, staining of starved H9C2 cells with the DX1 antibody revealed no signal (Figure S5), confirming the specificity of DX1 for ADN. However, in starved H9C2 cells exposed to the probe for 4 hours a strong signal was seen from both DX1 and Cy5.5. The degree of colocalization between the DX1 and Cy5.5 signal was extremely high (Figure S5) and the probe was highly aggregated in perinuclear lysosomes forming a large superparamagnetic nanoassembly. The flux of ADN can be clearly detected via its DX1 signal. Immediately after entry into the cell the probe is distributed very diffusely throughout the cytoplasm (main text, Figure 2K). Within 1 hour the probe has been taken up by LC3-GFP positive early autophagosomes (main text, Figure 2L) and has a more punctate/aggregated distribution. Four hours after probe exposure, reflecting the flux of the autophagosomes to the perinuclear lysosomes, ADN becomes extremely aggregated into a dense perinuclear nanoassembly (Figure S5).

The arginine-rich peptides on ADN play a key role in its detection with MRI by enhancing the direct entry of the probe into cells (Figure 2K),[8-10] promoting endosomal escape/release of any nanoparticles that enter the cell via endocytosis during autophagy,[11-14] and promoting the uptake of ADN by autophagosomes, which are highly avid for free nanoparticles in the cytoplasm,[12,15] and for polyarginine.[16,17] The uptake of ADN by autophagosomes results in their focal aggregation, which is further enhanced when the autophagosomes undergo flux to the lysosome (Figure S5). ADN in lysosomes thus exists in a very concentrated/aggregated distribution, which results in a significant increase in its magnetic relaxivity and detection by MRI. This phenomenon, where aggregated nanoparticles increase their relaxivity, has been termed the magnetic relaxation switch effect and forms the basis of numerous in vitro diagnostic tests.[6,7]
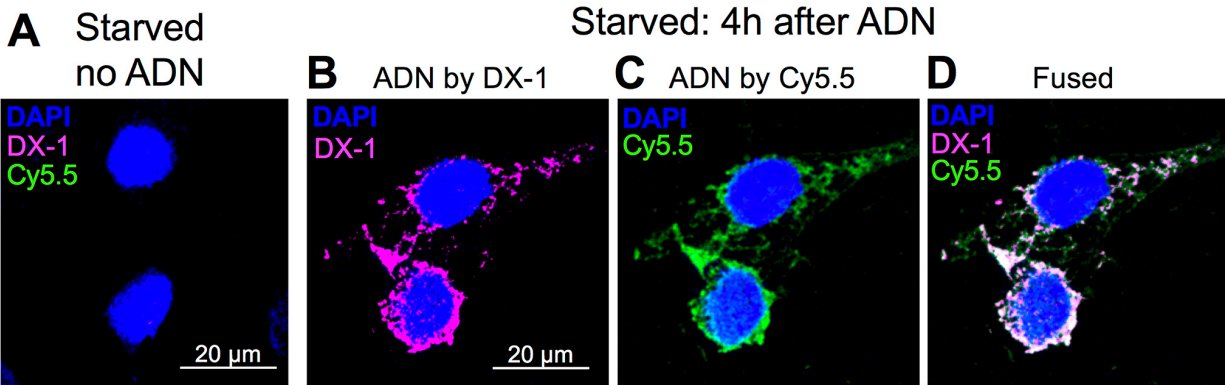
Figure S5. Detection of ADN in starved H9C2 cells 4 hours after probe exposure. A. In the absence of ADN no signal at all is seen with the DX1 antibody or in the Cy5.5 channel, confirming their specificity for ADN. **B-D.** Both the DX1 and Cy5.5 signals from ADN reveal that within 4 hours the probe is densely aggregated in perinuclear lysosomes. Three independent experiments were performed with consistent results.

Cardiomyocyte autophagy could be detected with ADN, both ex vivo and in vivo, by measuring the transverse magnetic relaxation rate (R2*) of the myocardium. Significant differences in R2* were seen with ADN between starved and fed mice (main text, Figure 3F-G, Figure 6L-M). In contrast, no significant differences in R2* between fed and starved mice could be detected with FH-Cy5.5, even ex vivo. This underscores the critical role of the arginine-rich peptides on ADN in probe detection by MRI. Interestingly, the fluorescent signal from ADN in starved H9C2 cells was significantly stronger than the signal from the free (non FH-bound) polyarginine-Cy5.5 construct (main text Figure 1J-K). The presence of both the FH and polyarginine moieties on ADN thus plays a key role in its detection by fluorescence as well as magnetic resonance.

6. Activation of ADN in Starved and Ischemic Myocardium

Starvation to the best of our knowledge does not produce an inflammatory cell infiltrate in the heart. However, to demonstrate definitively that the activation of ADN during starvation/nutrient deprivation was not due to an inflammatory response, the presence of CD68 positive cells in the myocardium was measured in starved mice (n=4). Mice with healing ischemic injury (n=3), studied 24 hours after ligation of the left coronary artery, served as the positive control.[18] CD68 fluorescence in the starved mice was similar to the uninjured septum (signal-to-noise ratios of 45.1 ± 1.2 and 46.5 ± 1.8), and was significantly lower than the signal in the area-at-risk (AAR)/infarct (51.6 ± 1.1) (Figure S6). Starvation was thus not associated with an inflammatory infiltrate, underscoring the specificity of ADN for cathepsin upregulation in cardiomyocytes during autophagy.

The mice with ischemia-reperfusion (IR) injury were imaged 4 hours after the onset of reperfusion, which is well before an inflammatory infiltrate develops.[19,20] Inflammation is also a potent activator of the cathepsin activatable fluorochrome (CAF, Prosense, Perkin Elmer) that was co-injected with ADN into the mice with IR.[21] Isolated activation of ADN

(without CAF activation) was seen in the first 4 hours of ischemia (main text, Figure 3A-C) indicating that the signal from ADN was indeed due to autophagy and not inflammation.
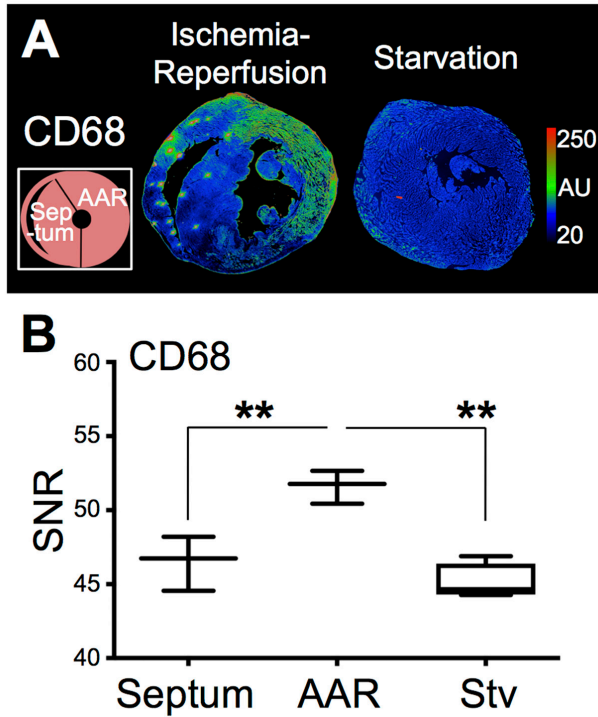
Figure S6: **Starvation does not produce an inflammatory infiltrate in the myocardium.** **A**. CD68 fluorescence microscopy of an infarcted mouse heart (left) and a mouse heart exposed to the starvation (Stv) protocol right. In the healing infarct a dense infiltrate of CD68-positive inflammatory cells (green) is seen in the ischemic area-at-risk (AAR) but not in the uninjured septum. Likewise, no evidence of inflammatory cells is seen in the starved heart. **B**. The intensity of CD68 fluorescence in the starved hearts was lower than the uninjured septum of the infarcted mice, and significantly lower than the injured myocardium in the area-at-risk (AAR). SNR = signal-to-noise ratio. N=3 (Septum), n=3 (AAR), and n=4 (Stv); **p=0.0070 (Septum vs. AAR), **p=0.0012 (AAR vs. Stv) by one-way ANOVA with Tukey post-test. Box plots show min, max, median and 25-75%.

7. Calculation of the Time Constant of Autophagic Flux

The ability to image ADN activation in the heart noninvasively allowed us to determine the in vivo time constant of autophagic flux (τ_{Flux}). 3D fluorescence imaging in starved mice, fused with x-ray CT, showed that the thoracic signal from ADN emanated from the heart. The 3D imaging experiments, however, were extremely time consuming (30 minutes per mouse) and were thus not suited to accurate kinetic modeling. In contrast, planar fluorescence reflectance imaging could be performed very rapidly and allowed each mouse to be imaged in increments as short as 5 minutes. Highly reproducible sternal fluorescence was seen in starved C57BL/6 mice injected with ADN, which allowed us to segment the left/right sides of the thorax and approximate the cardiac signal from the ratio of L/R thoracic fluorescence. Starved mice co-injected with ADN and bafilomycin showed no change in this L/R thoracic ratio, supporting its use to model ADN uptake in the heart (Figure 6, main text).

The cardiac (L/R ratio) signal in starved mice during the first 6 hours following ADN injection followed a mono-exponential growth curve with a plateau, as shown in Figure 6C-D of the main text. This can be described by:

$S = S_0(1 - e^{\frac{-t}{\tau_{ADN}}})$, where τ_{ADN} is the time constant of ADN signal growth in vivo.

We further modeled the signal from ADN over time using a 4-compartment model (Figure S7), in which ADN in the intravascular space moves across the endothelium into the interstitial space, and then crosses the cardiomyocyte cell membrane via a cellular

endosome/phagosome. The phagosome is subsequently trafficked to the lysosome and it is the flux of these phagosomes that plays such a crucial role in autophagy. Finally, within the lysosome, ADN is cleaved by cathepsins and other proteases and emits fluorescence. The activation of ADN is thus characterized by 4 sequential processes: i) movement across the endothelial membrane, ii) passage across the cell membrane, iii) phagosome flux to the lysosome and, iv) cleavage and activation of ADN within the lysosome. Experimental data showed that each of these processes could be described by a plateaued mono-exponential growth function, each having its own time constant (τ).
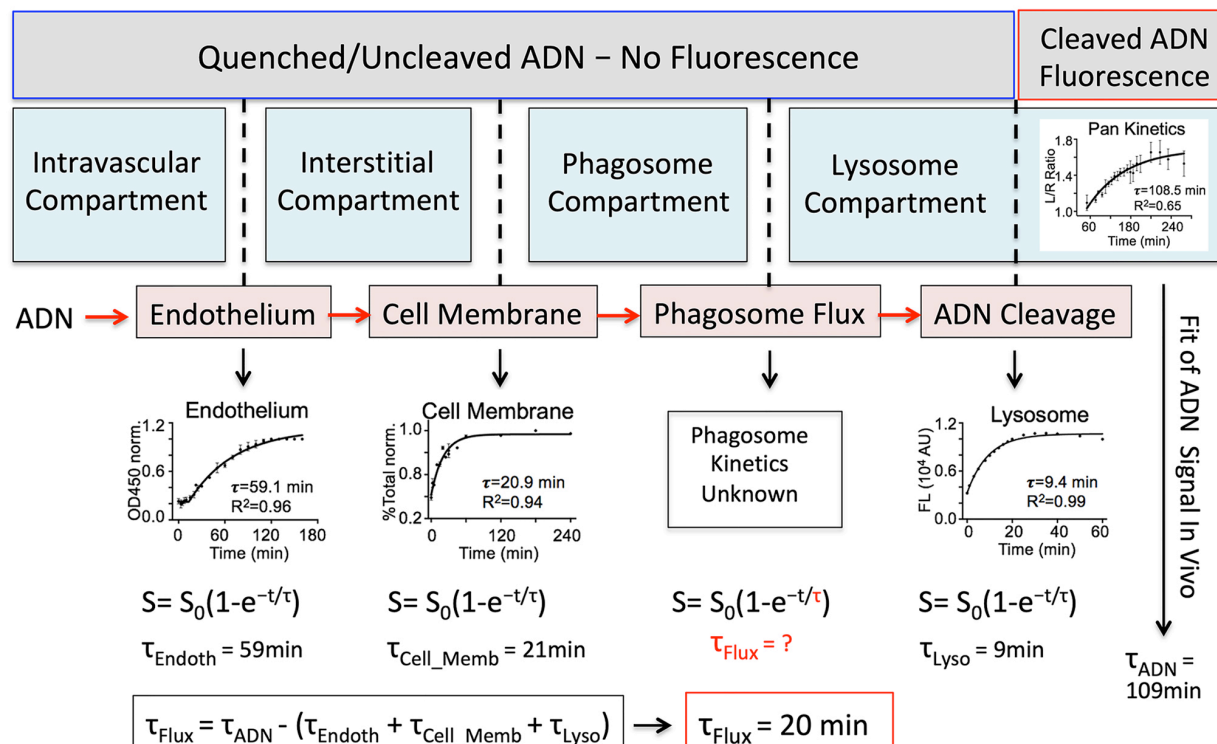
Figure S7: **Kinetic model of ADN activation in the heart in vivo.** The kinetic curves shown here are also shown in Figure 6 of the main text. Four processes must occur for ADN to emit fluorescence: Passage across the endothelium, passage across the cardiomyocyte cell membrane via a phagosome, flux of the phagosome to the lysosome, and cleavage of ADN by lysosomal cathepsins. Other than flux, the time constants of these processes, which all follow plateaued exponential growth, can be measured in vitro. The kinetics of ADN signal growth in the heart can be measured in vivo, which allows an estimate of in vivo autophagic flux (τ_{Flux}) to be obtained.

The calculation of autophagic flux, above, assumes that the passage of ADN across the endothelium and cardiomyocyte membranes, as well as its cleavage by lysosomal cathepsins, all have similar rates in vivo and vitro. In addition, the proposed kinetic model is unidirectional at all steps. This, as discussed below, is a reasonable assumption since FH does not display a reverse vascular phase and the cleavage of ADN is irreversible.

8. Modeling of Autophagosome Number and Flux

Further quantification of autophagic flux was performed using a four-compartment (three-tissue compartment) in series model, as shown in Figure S7 and in Figure S8 below. The aim of this analysis was to determine the number of autophagosomes that would move into the lysosomal compartment in response to starvation. Hitherto, the key kinetic constant in the model k_5, which describes the flux of autophagosomes to the lysosome, would need to be estimated from in vitro observations. Here, using in vivo imaging data, τ_{Flux} is used to directly derive k_5 (Figure S8A-B).

ADN is not taken up by red blood cells and is distributed after intravenous injection into the plasma compartment of the intravascular space. Based on the injected dose of ADN (10mg Fe/kg), the molecular weight of FH and hence ADN in Fe (328,944 Daltons) and an average plasma volume per mouse of 1.675ml,[22] the initial concentration (I) of ADN in the plasma was calculated as 2.731×10^{14} nanoparticles/ml. The intravascular kinetics of ADN were measured through absorption spectrophotometry (of iron) in plasma samples derived from serial blood draws. This showed that ADN levels followed a mono-exponential decay with a half-life of 50.7 min (Table S1) or time constant (τ_p) of 74 minutes, which was used to model ADN concentration over time in the intravascular (plasma) compartment (C_a) as follows:

$$C_a(t) = I * e^{\frac{-t}{\tau_p}}$$
Eq. 1

The movement of ADN across the endothelial membrane and into the interstitial compartment (C_1) was calculated using the Renkin-Crone capillary model to relate the kinetic rate constant K_1 (ml/g/min) to the extraction fraction (E) and plasma flow (F).[23]

$$K_1 = EF = \left(1 - e^{\frac{-ps}{F}}\right) F$$
Eq. 2

Where F is the flow of plasma in the myocardium, p is the permeability constant and s is the capillary surface area. Previously published values of resting myocardial blood flow in the murine heart (6-7 ml/g/min) using arterial spin labeling,[24-26] were used to derive a lower limit of F (3ml/g/min). Likewise, published values for capillary surface area in rodent myocardium (77.49 mm^2/mm^3 or 817.5 cm^2/g),[27] and the permeability of 20nm sized nanoparticles (1.8×10^{-6} cm/s or 1.08×10^{-4} cm/min),[28] were used to derive K_1. The removal of iron-oxide nanoparticles, such as ADN, from the interstitial space into the lymph (k_2) occurs via very slow transport mechanisms.[29] The value of k_2 over the time course (0-4 hours) modeled here is thus negligible and was set to zero.

The movement of ADN across the cell membrane and into the phagosome compartment is described by k_3 (Figure S8), and the potential secretion of ADN out of the cell via exocytosis by k_4. While exocytosis of autophagosomes has been described in some contexts, deprivation of amino-acids during autophagy severely/completely inhibits secretion from the cell,[30] and k_4 was thus set to zero. The calculation of k_3 was based on published studies in which 10^6 mesenchymal stem cells were incubated for approximately 180 min in medium containing 200 ug Fe/ml of ferumoxytol and polyarginine (protamine).[31] Since the specific gravity of these media is extremely close to 1, this can also be expressed as the amount of ferumoxytol and number of cells (n) per gram of

medium. The average amount of iron accumulation per cell was 7.23 pg, which in 1g of medium (n = 10^6 cells) creates an intracellular/extracellular iron ratio of 7.23 ug /200 ug and, over the 180 min exposure time, a k_3 (min^{-1}) value of 2.0×10^{-4}. The concentration of ADN in the interstitial compartment (C_1) is thus described by:

$$\frac{d}{dt}C_1(t) = K_1 C_a(t) - k_3 C_1(t) \qquad \text{Eq. 3}$$

Application of a Laplace transform to Eq. 3 yields:

$$S\overline{C_1(S)} = K_1 \overline{C_a(S)} - k_3 \overline{C_1(S)} \qquad \text{Eq. 4}$$

The inverse Laplace transform of Eq. 4 yields:

$$C_1(t) = K_1 C_a(t) \otimes e^{-k_3 t} \qquad \text{Eq. 5}$$

Where, the symbol $\otimes$ denotes convolution, and K_1 and C_a are provided from equations 1 and 2 above.

The time constant of autophagic flux (τ_{Flux}) in starved myocardium, derived above, was then used to estimate the kinetic rate constant (k_5) of autophagic flux into the lysosome. Allowing 5 times tau (τ) for a plateaued exponential growth curve to complete its growth ($5\tau_{\text{Flux}}$ = 100 min), an average k_5 of 0.01 min^{-1} was derived. The secretion of intact ADN from the lysosome back into the cytoplasm has not been documented and k_6 was thus set to zero. The concentration of ADN in the phagosome compartment (C_2) is thus described by:

$$\frac{d}{dt}C_2(t) = k_3 C_1(t) - k_5 C_2(t) \qquad \text{Eq. 6}$$

As above, the use of the Laplace transform and its inverse can be used to derive the following equations:

$$S\overline{C_2(S)} = k_3 \overline{C_1(S)} - k_5 \overline{C_2(S)} \qquad \text{Eq. 7}$$
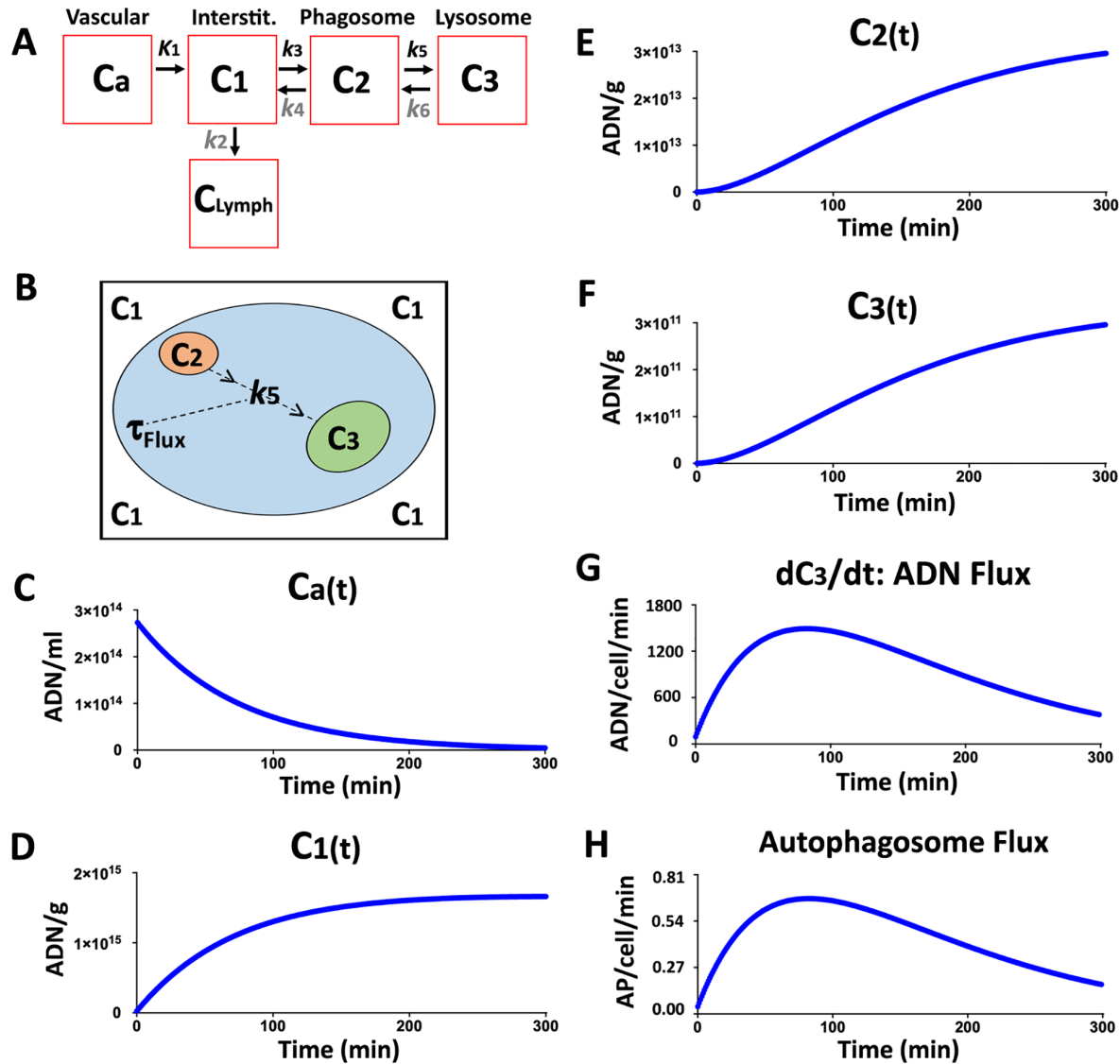
$$C_2(t) = k_3 C_1(t) \otimes e^{-k_5 t} \qquad \text{Eq. 8}$$

Likewise, the concentration of ADN in the lysosome compartment (C_3) can be derived as follows:

$$\frac{d}{dt}C_3(t) = k_5 C_2(t) \qquad \text{Eq. 9}$$

$$S\overline{C_3(S)} = k_5 \overline{C_2(S)} \qquad \text{Eq. 10}$$

$$C_3(t) = k_5 C_2(t) \qquad \text{Eq. 11}$$

Figure S8: Quantification of autophagic flux. A. Multicompartment model of autophagic flux where Ca is the concentration of ADN in the intravascular compartment, C_1 ADN concentration in the interstitial compartment, C_2 concentration in the phagosome compartment and C_3 ADN concentration in the lysosome compartment. The kinetic constants describe the rate of movement between the various compartments: k_2, k_4 and k_6 are negligible and are set to zero. **B**. The kinetic constant k_5, which describes autophagic flux to the lysosome, is derived from τ_{Flux}, which in turn is calculated from serial in vivo imaging data. **C**. The concentration of ADN in the intravascular compartment follows a mono-exponential decay. **D**. The concentration of ADN in the interstitial compartment plateaus within 4 hours of injection. **E-F**. ADN concentrations in the phagosome (C_2) and lysosome (C_3) compartments are several orders of magnitude lower than C_1 and take more time to rise. **G**. The flux of ADN per cell is calculated as $(dC_3/dt)/n$, where n = the number of cells in the model. ADN flux, and hence autophagic flux, peaks 80-90 minutes after probe injection. **H**. The peak increase in autophagic flux above baseline is > 40 per hour and the total number of autophagosomes that undergo flux to the lysosome in response to starvation (area-under-the-curve-AUC) is > 130. AP = autophagosome.

Testing of the model revealed that it was highly stable over a broad range of plasma flow rates. This is key since myocardial blood flow in mice varies significantly (5-12 ml/kg/min) with the dose of inhaled isoflurane,[24-26,32] and hematocrit can vary widely too. No significant difference (<1%) was seen in autophagic flux with plasma flow rates (F) ranging from 3-7 ml/g/min. One of the limitations, however, of kinetic modeling with ADN lies in its inability to detect the baseline level of autophagy in normally fed hearts in vivo. In fed mice the fluorescence signal after ADN injection remains at a low constant level, with τ_{Fed} thus trending to infinity and k_{5Fed} trending to zero. The time constant of autophagic flux (τ_{Flux}) and the kinetic rate constant k_5, modeled here, thus represent the difference or increase in flux, produced by starvation, above the baseline level.

As shown in Figure S8F, our model suggests that almost 3×10^{11} ADN nanoparticles/gram accumulate in the lysosomal space of the myocardium in a starved mouse 4 hours after probe injection. Since the concentration/aggregation of superparamagnetic nanoparticles in lysosomes causes a major increase in their magnetic relaxivity (r2*), also known as a magnetic relaxation switch effect,[6] this degree of nanoparticle accumulation could be well detected by R2* mapping (see Figures 3F-G and 6L-M main text). The rate of ADN accumulation (flux) is calculated as dC_3/dt and reaches a peak value of 1.492×10^9 nanoparticles/g/min between 80-90 minutes after probe injection (Figure S8G). Conversion of peak flux from a per gram to a per cell basis is achieved by dividing by the number of cells (n = 10^6) used in the calculation of k_3, producing a peak flux per cell of 1492 ADN nanoparticles/min.

We next convert the flux of ADN nanoparticles to the flux of autophagosomes. Electron microscopy of cells exposed to ferumoxytol ± polyarginine has shown approximately 50 nanoparticles per section (average thickness 60nm),[3] in endosomes that are approximately 500nm in diameter (50 nanoparticles per $1.178\times10^7 nm^3$).[3,4] The size of autophagosomes in mammalian cells ranges from 500 to 1500nm,[33] and an average autophagosome diameter in the cardiomyocyte of 1000nm and volume of $5.235\times10^8 nm^3$ was thus assumed. Assuming the concentration of nanoparticles in autophagosomes is similar to that in endosomes, there are approximately 2220 ADN nanoparticles per autophagosome. The peak increase in autophagic flux above baseline levels = 1492/2220 per minute/cell or 40.3 autophagosomes per hour per cell. The total number of autophagosomes per cell undergoing flux to the lysosomal compartment in response to starvation (area-under-the curve, AUC, over 5hrs in Figure S8H) reaches approximately 133. These values are similar to the increase in flux noted in vitro in rapamycin-treated cells,[34] but are derived here using an in vivo imaging approach. Our approach allows τ_{Flux} to be imaged in any mouse model in vivo and, subsequently, for peak and total autophagic flux in the heart to be calculated. This could facilitate an improved understanding of autophagy and guide the development of therapies to modulate the process.

9. Autophagy Modulation Attenuates Dasatinib Toxicity

Numerous chemotherapeutic drugs, in addition to doxorubicin (Dox), can exert cardiotoxic effects. To demonstrate that ADN can be broadly used to characterize the role of

autophagy during chemotherapy with any class of agent, we chose to study the tyrosine kinase inhibitor dasatinib.

Tyrosine Kinase Inhibitor: Dasatinib

We next chose to study the second-generation tyrosine kinase inhibitor (TKI) dasatinib, which has been linked to pulmonary hypertension but may also damage cardiomyocytes and cause heart failure.[35,36] Dasatinib (DAS) incubation for 24 hours in H9C2 cells significantly reduced ADN fluorescence by FACS (Figure S9A-B), which was associated with a two-fold reduction in cell survival (Figure S9C). The addition of either atorvastatin or simvastatin returned the level of autophagy flux (ADN positive population) during DAS exposure back to baseline (Figure S9B). In addition, as shown in Figure S9C, the addition of atorvastatin or simvastatin was associated with a marked improvement in cell survival (98.4%±23.0% and 90.4%±20.3%, respectively, p<0.01 vs. DAS alone). The rescue of autophagy during DAS exposure by rapamycin had a similar protective effect (Figure S9D), while the inhibition of autophagy by bafilomycin markedly reduced H9C2 survival.
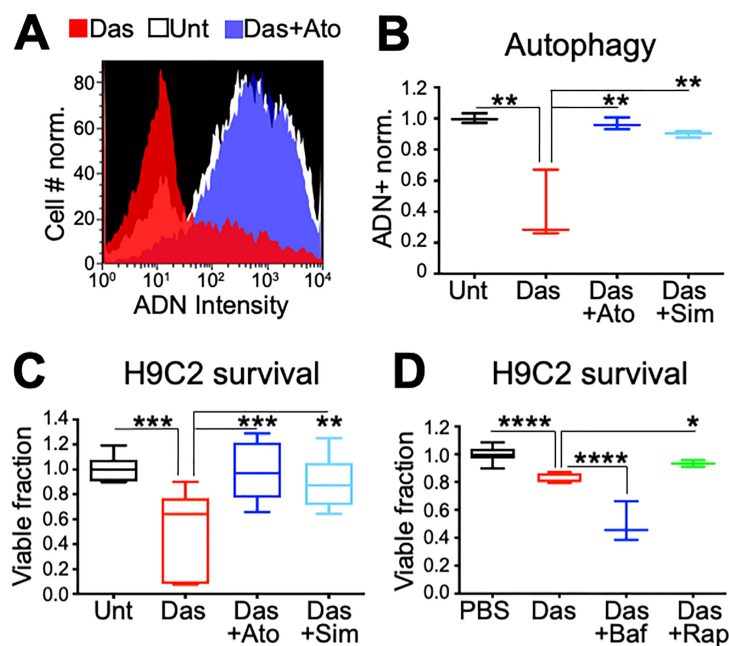
Figure S9: Modulation of autophagy enhances H9C2 cardiomyocyte survival after exposure to a tyrosine kinase inhibitor. A-B. Dasatinib markedly reduces ADN activation in H9C2 cardiomyocytes, however, baseline levels of autophagy can be restored by co-exposure to atorvastatin (Ato) or simvastatin (Sim). n=3 in each group, **p=0.0012 comparing untreated (Unt) to dasatinib only (Das), **p=0.0018 comparing Das to Das+Ato, **p=0.0040 comparing Das to Das+Sim, by one-way ANOVA with Tukey post-test. Box plots show min, max and median. **C.** The restoration of basal autophagy levels by statins is associated with improved survival (viability by MTT) in H9C2s exposed to dasatinib. n=9 per group, ***p=0.0004 comparing Unt to Das, ***p=0.0006 comparing Das to Das+Ato, **p=0.0048 comparing Das to Das+Sim, by one-way ANOVA with Tukey post-test. Box plots show min, max, median and 25-75%. **D**. A similar protective effect is seen with rapamycin and the opposite effect with bafilomycin. n=12 (PBS), n=9 (Das), n=3 (Das+Baf), n=3 (Das+Rap), *p=0.0450 comparing Das to Das+Rap, **** p<0.0001, by one-way ANOVA with Tukey post-test. Box plots show min, max, median and 25-75%.

The response of cardiomyocytes to DAS and Dox was thus very similar. Collectively these data show that the dysregulation of autophagy may contribute to the toxicity of a broad range of chemotherapeutic agents. Moreover, the stimulation of autophagy has the potential to be highly cardioprotective.

10. Supplementary Methods

Reagents. Clinically used agents including ferumoxytol, dasatinib, atorvastatin, and simvastatin were purchased from the research pharmacy at the Massachusetts General Hospital and Tufts Medical Center. Chemicals for ADN synthesis include Hydroxybenzotriazole (TCI America, Tokyo Japan; product number H0468), 1-Ethyl-3-(3-dimethylaminopropyl) carbodiimide (EMD Millipore; Burlington MA; catalog number 01-62-0011), MES sodium salt (Sigma-Aldrich, St. Louis MO; SKU M5057), Cy5.5 NHS ester (Lumiprobe, Hunt Valley MD; catalog number 57020), DBCO-PEG4-Maleimide (Click Chemistry Tools, Scottsdale AZ; catalog number A108P), Azido-PEG3-Amine (Click Chemistry Tools, Scottsdale AZ; catalog number: AZ101-100), Cy5.5-DBCO (Lumiprobe; catalog number: B70F0). Immortalized cell lines acquired from ATCC (Manassas VA) were rat cardiac H9C2 cells (catalog number CRL-1446), and the human breast cancer cell lines MCF7 (catalog number HTB-22) and MDA-MB-231 (catalog number HTB-26). Fluorescent LC3 plasmids (Addgene, Watertown MA; catalogue number 21074 and 84572) were transfected with lipofectamine (Thermo Fisher Scientific, Waltham MA; catalog number L3000008). The antibodies used for immunostaining (Cell Signaling Technology, Danvers MA) were specific for LC3B (catalog number 3868, clone: D11, 1:1000 dilution), p62 (catalog number 5114, 1:1000 dilution), GAPDH (catalog number 2118, clone: 14C10, 1:1000 dilution), and (from Sigma, Burlington MA) β-Actin (catalog number A5316, clone: AC-74, 1:5000 dilution). Anti-dextran DX-1 antibody (catalog number 60026, clone: DX1, 1:100 dilution) was purchased from STEMCELL Technologies (Vancouver, Canada). Fluorescent anti-mouse IgG-Alexa Fluor 790 secondary antibody (catalog number 715-655-151) was purchased from Jackson Immuno (West Grove, PA). Fluorescent Annexin V for in vivo imaging was purchased from Perkin Elmer (Waltham MA; Part number NEV11053). Atg7 DsiRNAi (forward oligo: GUGAUUUCUUCCAAGGUCAAAGGAC and reverse oligo: GUCCUUUGACCUUGGAAGAAAUCACUG) and negative control non-coding DsiRNA (catalog number 51-01-14-04) were purchased from Integrated DNA Technologies (Coralville, IA). Additional chemicals include rapamycin (Cayman Chemical, Ann Arbor MI; item number 13346), bafilomycin A1 (Cayman Chemical; item number 11038), E-64d (Sigma-Aldrich; SKU E8640), pepstatin A (Sigma-Aldrich; SKU 77170), doxorubicin (Cayman Chemical; item number 15007), and the cell viability dye methylthialazole tetrazolium (MTT; Cayman Chemical; item number 21795). Male and female C57BL/6 mice between 8-10 weeks of age were purchased from the Jackson Laboratory (Bar Harbor ME).

Cell viability MTT assay. The survival and viability of cells was measured with a MTT (dimethylthiazol) assay (Sigma). The assay was prepared according to a well-established protocol with the following specifications. Briefly, cells were plated on 96-well plates at 2.5×10^4 cells/well, and placed into a 37ºC, 5% CO2, incubator for 24 hours. The next day, the cell medium was replaced by fresh cell culture medium, at which time various concentrations of Dox were added for a further 24 hours of incubation. Thereafter, the Dox containing medium was removed and 100 µL of MTT prepared at 0.5 mg/mL in phenol red free, serum free DMEM solutions was added to the cells for an additional 2 hours. The MTT solution was then removed and 100 µL of MTT solvent (4mM HCL+0.1%

NP-40+ isopropanol) was added to the plate for 30 min. Finally, a microplate reader was used to determine absorbance at 590 nm.

Protein immunoblot. H9C2 cells were washed with 1x cold PBS, and the lysates were prepared on ice in RIPA (radio-immunoprecipitation assay) buffer supplemented with a cocktail of protease inhibitors. Proteins were extracted by constant agitation for 30 minutes before centrifugation to collect the supernatant. Protein concentration was measured by Bradford assay (BioRad), and 20-40 µg of total protein was loaded for electrophoresis and transferred to the polyvinylidene difluoride (PVDF) membrane. Then, the membrane was processed for immunoblotting and imaged with a ChemiDoc XRS molecular imager (BioRad).

Transmission electron microscopy of ADN. Transmission electron microscopy (TEM) was performed in H9C2 cells pre-starved for 23 hours before the addition of either ADN (10 µg Fe/ml) or PBS (control) for 1 additional hour. The cells were fixed with a modified Karnovsky's solution (2% paraformaldehyde /2.5% glutaraldehyde in 0.1M sodium cacodylate buffer, pH 7.4) and rinsed in 0.1M cacodylate buffer. The pelleted cells were post-fixed for 1hr in 1% OsO_4/0.1M cacodylate buffer, then rinsed again several times in 0.1M cacodylate buffer, re-centrifuging as needed to keep the pellet aggregate together. The pellets were embedded in 2% agarose, and dehydrated in 30% ethanol for 30min. The pellets were further dehydrated through a graded series of ethanols to 100% as follows: 50%, 70%, 80%, 90% - 20min each step, then in 95% & 100% ethanol - 15min each step. The specimens were briefly dehydrated in 100% propylene oxide, then allowed to infiltrate overnight in a 1:1 mix of propylene oxide and Eponate resin (Ted Pella, Redding, CA) on a gentle rotator.

The following day, samples were allowed to infiltrate for several hours in fresh 100% Eponate resin. The agarose blocks were embedded in flat molds in 100% fresh Eponate resin and allowed to polymerize for 24-48hrs at 60°C. Thin (70nm) sections were cut using a Leica EM UC7 ultramicrotome, collected onto formvar-coated grids, stained with 2% uranyl acetate and Reynold's lead citrate and examined in a JEM 1011 (JEOL, Peabody MA) transmission electron microscope at 80 kV. Images were collected using an AMT digital imaging system with proprietary image capture software (Advanced Microscopy Techniques, Danvers, MA).

Endothelial passage of ADN. The time constant of ADN translocation across an endothelial membrane was measured in a two-chamber well system, separated by a transwell insert (Corning, Corning NY). Human umbilical vein endothelial cells (HUVECs, $5x10^4$ cells) were plated on transwell inserts with a 0.4 µm permeable polycarbonate membrane and pre-coated with matrigel basement membrane matrix (Corning, Corning NY) prepared 1:60 in PBS. The cells were allowed to grow overnight under optimal conditions in order to attach and form a confluent layer, separating the two chambers. The medium in the well was then changed to expose the endothelial layer to 24 hours of nutrient free conditions (starvation) before ADN (10 µg/ml) was added to the apical chamber. Samples in the basolateral chamber were collected at discrete time intervals,

and ADN content in these samples was measured by absorbance spectroscopy for iron content at 450 nm on a Nanodrop 2000c spectrophotometer (Thermo Scientific).

Echocardiography imaging. Transthoracic echocardiographic imaging was performed with a 13.0-MHz linear probe (Vevo 2100 system; VisualSonics, Toronto Canada) and analyzed by 2 experienced echocardiographers blinded to the experimental design. Briefly, mice were lightly anesthetized with isoflurane and positioned on heated stage with ECG monitoring before M-mode images of the left ventricle were obtained at the level of the papillary muscles. Left ventricular diameter was used to calculate stroke volume and cardiac output. Strain analysis was performed with VivoStrain (VisualSonics) on three consecutive cardiac cycles and the values were averaged.

References:

1   Tesei, G. *et al.* Self-association of a highly charged arginine-rich cell-penetrating peptide. *Proc Natl Acad Sci U S A* **114**, 11428-11433, doi:10.1073/pnas.1712078114 (2017).

2   Zhou, J. *et al.* Activation of lysosomal function in the course of autophagy via mTORC1 suppression and autophagosome-lysosome fusion. *Cell Res* **23**, 508-523, doi:10.1038/cr.2013.11 (2013).

3   Thu, M. S. *et al.* Self-assembling nanocomplexes by combining ferumoxytol, heparin and protamine for cell tracking by magnetic resonance imaging. *Nat Med* **18**, 463-467, doi:10.1038/nm.2666 (2012).

4   Liu, L. *et al.* A New Method for Preparing Mesenchymal Stem Cells and Labeling with Ferumoxytol for Cell Tracking by MRI. *Sci Rep* **6**, 26271, doi:10.1038/srep26271 (2016).

5   McConnell, H. L. *et al.* Ferumoxytol nanoparticle uptake in brain during acute neuroinflammation is cell-specific. *Nanomedicine* **12**, 1535-1542, doi:10.1016/j.nano.2016.03.009 (2016).

6   Perez, J. M., Josephson, L., O'Loughlin, T., Hogemann, D. & Weissleder, R. Magnetic relaxation switches capable of sensing molecular interactions. *Nat Biotechnol* **20**, 816-820, doi:10.1038/nbt720 (2002).

7   Taktak, S., Sosnovik, D., Cima, M. J., Weissleder, R. & Josephson, L. Multiparameter magnetic relaxation switch assays. *Anal Chem* **79**, 8863-8869, doi:10.1021/ac701976p (2007).

8   Lewin, M. *et al.* Tat peptide-derivatized magnetic nanoparticles allow in vivo tracking and recovery of progenitor cells. *Nat Biotechnol* **18**, 410-414, doi:10.1038/74464 (2000).

9   Nakase, I. *et al.* Arginine-rich cell-penetrating peptide-modified extracellular vesicles for active macropinocytosis induction and efficient intracellular delivery. *Sci Rep* **7**, 1991, doi:10.1038/s41598-017-02014-6 (2017).

10   Schmidt, N., Mishra, A., Lai, G. H. & Wong, G. C. Arginine-rich cell-penetrating peptides. *FEBS Lett* **584**, 1806-1813, doi:10.1016/j.febslet.2009.11.046 (2010).

11   Appelbaum, J. S. *et al.* Arginine topology controls escape of minimally cationic proteins from early endosomes to the cytoplasm. *Chem Biol* **19**, 819-830, doi:10.1016/j.chembiol.2012.05.022 (2012).

12   Kobayashi, S. *et al.* Artificial induction of autophagy around polystyrene beads in nonphagocytic cells. *Autophagy* **6**, 36-45, doi:10.4161/auto.6.1.10324 (2010).

13   Najjar, K. *et al.* Unlocking Endosomal Entrapment with Supercharged Arginine-Rich Peptides. *Bioconjug Chem* **28**, 2932-2941, doi:10.1021/acs.bioconjchem.7b00560 (2017).

14   Qian, Z. *et al.* Early endosomal escape of a cyclic cell-penetrating peptide allows effective cytosolic cargo delivery. *Biochemistry* **53**, 4034-4046, doi:10.1021/bi5004102 (2014).

15   Remaut, K., Oorschot, V., Braeckmans, K., Klumperman, J. & De Smedt, S. C. Lysosomal capturing of cytoplasmic injected nanoparticles by autophagy: an additional barrier to non viral gene delivery. *J Control Release* **195**, 29-36, doi:10.1016/j.jconrel.2014.08.002 (2014).

16   Dowaidar, M. *et al.* Role of autophagy in cell-penetrating peptide transfection model. *Sci Rep* **7**, 12635, doi:10.1038/s41598-017-12747-z (2017).

17   Robison, A. D. *et al.* Polyarginine Interacts More Strongly and Cooperatively than Polylysine with Phospholipid Bilayers. *J Phys Chem B* **120**, 9287-9296, doi:10.1021/acs.jpcb.6b05604 (2016).

18   Chen, H. H. *et al.* Theranostic Nucleic Acid Binding Nanoprobe Exerts Anti-inflammatory and Cytoprotective Effects in Ischemic Injury. *Theranostics* **7**, 814-825, doi:10.7150/thno.17366 (2017).

19   Nahrendorf, M. *et al.* The healing myocardium sequentially mobilizes two monocyte subsets with divergent and complementary functions. *J Exp Med* **204**, 3037-3047, doi:10.1084/jem.20070885 (2007).

20   Chen, H. H. *et al.* Fluorescence tomography of rapamycin-induced autophagy and cardioprotection in vivo. *Circ Cardiovasc Imaging* **6**, 441-447, doi:10.1161/CIRCIMAGING.112.000074 (2013).

21   Nahrendorf, M. *et al.* Dual channel optical tomographic imaging of leukocyte recruitment and protease activity in the healing myocardial infarct. *Circ Res* **100**, 1218-1225, doi:10.1161/01.RES.0000265064.46075.31 (2007).

22   Kaliss, N. & Pressman, D. Plasma and blood volumes of mouse organs, as determined with radioactive iodoproteins. *Proc Soc Exp Biol Med* **75**, 16-20, doi:10.3181/00379727-75-18083 (1950).

23   Di Rocco, R. J. *et al.* The single-pass cerebral extraction and capillary permeability-surface area product of several putative cerebral blood flow imaging agents. *J Nucl Med* **34**, 641-648 (1993).

24   Kober, F., Iltis, I., Cozzone, P. J. & Bernard, M. Myocardial blood flow mapping in mice using high-resolution spin labeling magnetic resonance imaging: influence of ketamine/xylazine and isoflurane anesthesia. *Magn Reson Med* **53**, 601-606, doi:10.1002/mrm.20373 (2005).

25   Streif, J. U. *et al.* In vivo assessment of absolute perfusion and intracapillary blood volume in the murine myocardium by spin labeling magnetic resonance imaging. *Magn Reson Med* **53**, 584-592, doi:10.1002/mrm.20327 (2005).

26   Naresh, N. K. *et al.* Repeatability and variability of myocardial perfusion imaging techniques in mice: Comparison of arterial spin labeling and first-pass contrast-enhanced MRI. *Magn Reson Med* **75**, 2394-2405, doi:10.1002/mrm.25769 (2016).

27   Warley, A., Powell, J. M. & Skepper, J. N. Capillary surface area is reduced and tissue thickness from capillaries to myocytes is increased in the left ventricle of streptozotocin-diabetic rats. *Diabetologia* **38**, 413-421, doi:10.1007/BF00410278 (1995).

28   Ho, Y. T. *et al.* A Facile Method to Probe the Vascular Permeability of Nanoparticles in Nanomedicine Applications. *Sci Rep* **7**, 707, doi:10.1038/s41598-017-00750-3 (2017).

29   Normandin, M. D. *et al.* Heat-Induced Radiolabeling of Nanoparticles for Monocyte Tracking by PET. *Angew Chem Int Ed Engl* **54**, 13002-13006, doi:10.1002/anie.201505525 (2015).

30   van Leeuwen, W., van der Krift, F. & Rabouille, C. Modulation of the secretory pathway by amino-acid starvation. *J Cell Biol* **217**, 2261-2271, doi:10.1083/jcb.201802003 (2018).

31   Bryant, L. H., Jr. *et al.* Physicochemical characterization of ferumoxytol, heparin and protamine nanocomplexes for improved magnetic labeling of stem cells. *Nanomedicine* **13**, 503-513, doi:10.1016/j.nano.2016.07.011 (2017).

32   Campbell-Washburn, A. E. *et al.* Cardiac arterial spin labeling using segmented ECG-gated Look-Locker FAIR: variability and repeatability in preclinical studies. *Magn Reson Med* **69**, 238-247, doi:10.1002/mrm.24243 (2013).

33   Mizushima, N., Ohsumi, Y. & Yoshimori, T. Autophagosome formation in mammalian cells. *Cell Struct Funct* **27**, 421-429, doi:10.1247/csf.27.421 (2002).

34   du Toit, A., De Wet, S., Hofmeyr, J. S., Muller-Nedebock, K. K. & Loos, B. The Precision Control of Autophagic Flux and Vesicle Dynamics-A Micropattern Approach. *Cells* **7**, doi:10.3390/cells7080094 (2018).

35   Hasinoff, B. B., Patel, D. & Wu, X. The Myocyte-Damaging Effects of the BCR-ABL1-Targeted Tyrosine Kinase Inhibitors Increase with Potency and Decrease with Specificity. *Cardiovasc Toxicol* **17**, 297-306, doi:10.1007/s12012-016-9386-7 (2017).

36   Chaar, M., Kamta, J. & Ait-Oudhia, S. Mechanisms, monitoring, and management of tyrosine kinase inhibitors-associated cardiovascular toxicities. *Onco Targets Ther* **11**, 6227-6237, doi:10.2147/OTT.S170138 (2018).
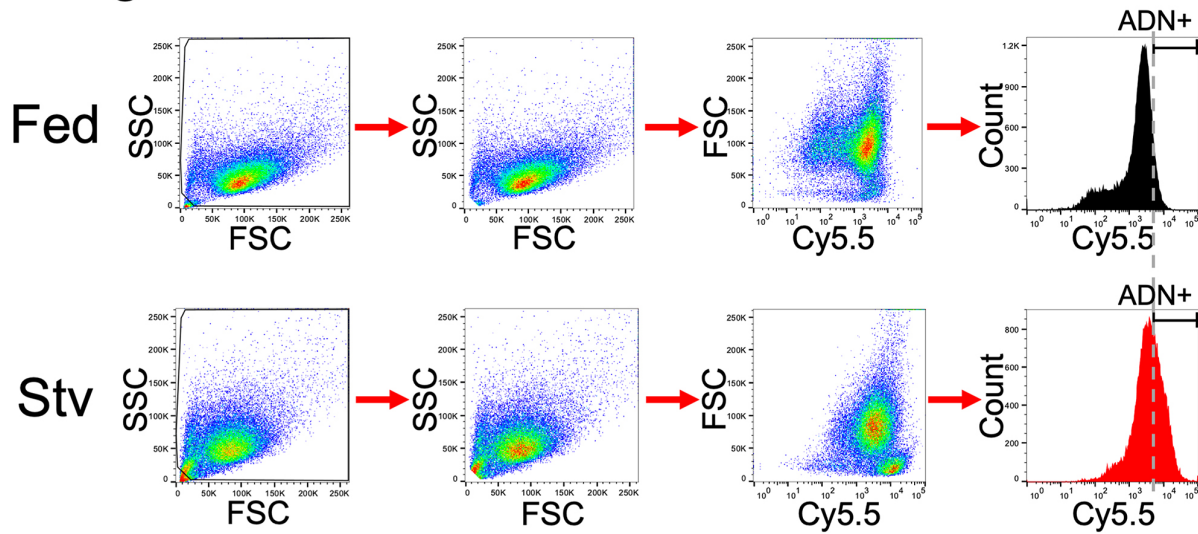
11. Supplementary Data

Figure S3B
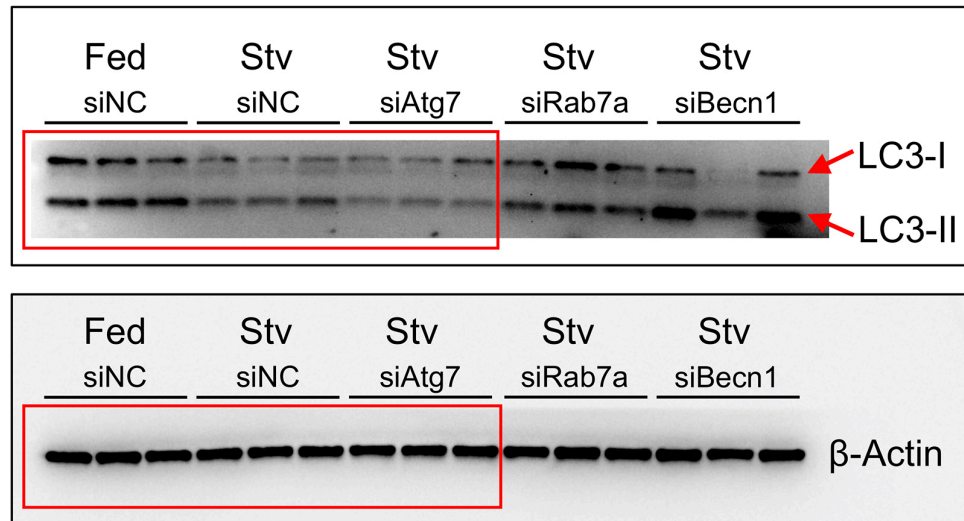
Uncropped Gel from Supplementary Fig. S3B
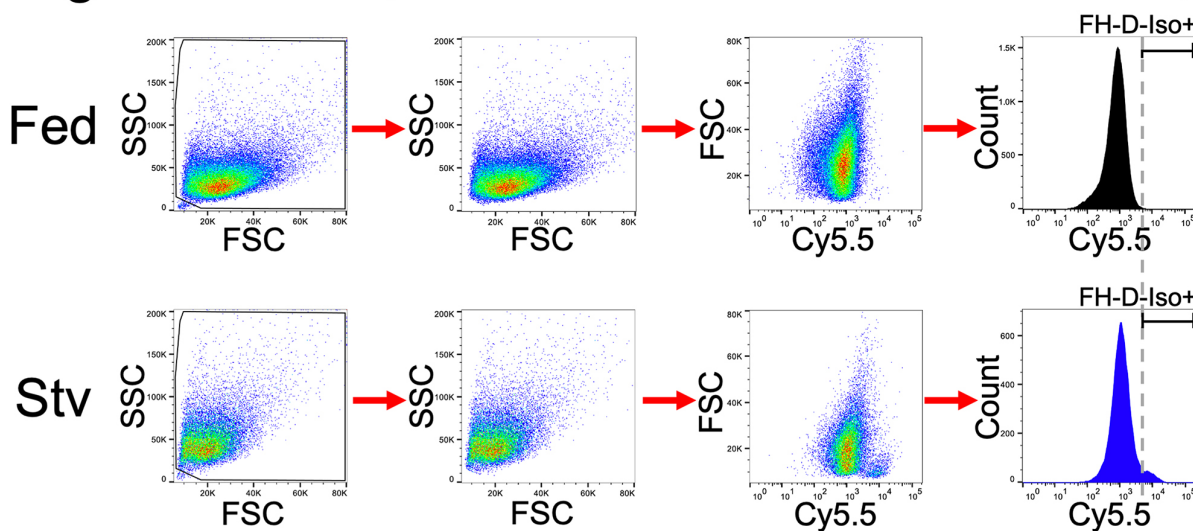
Figure S9A-B   H9C2 cells Das vs. Das+Ato: ADN
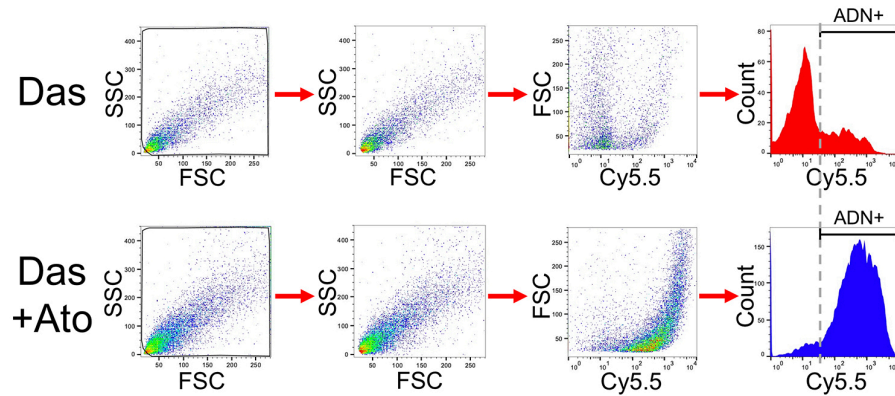
Gating strategy for Supplementary Fig. S9A-B

Figure 2C-D (H9C2 cells Fed vs. Stv: ADN)
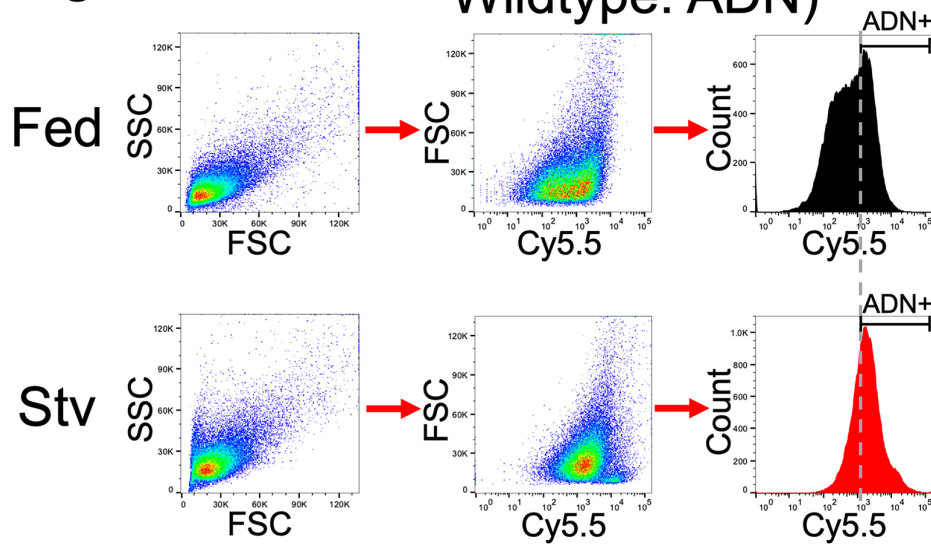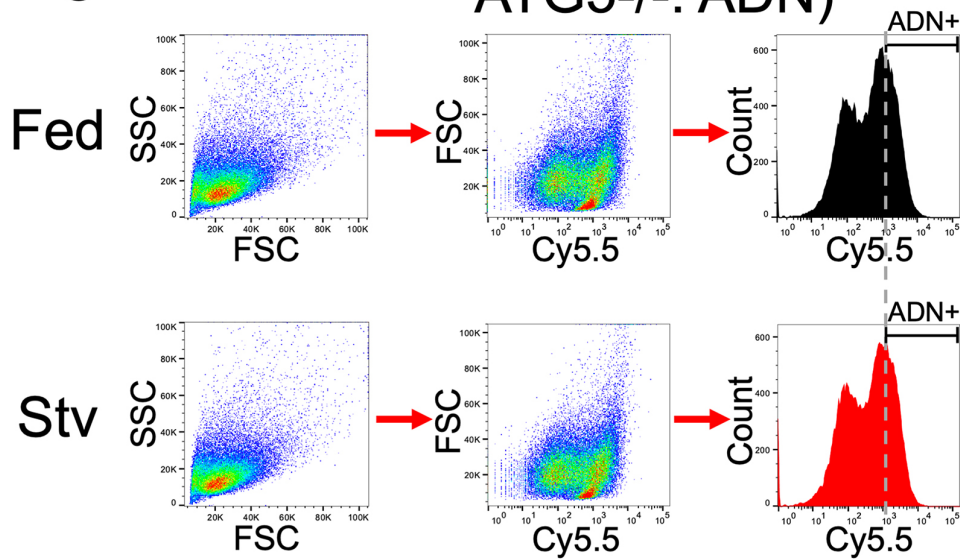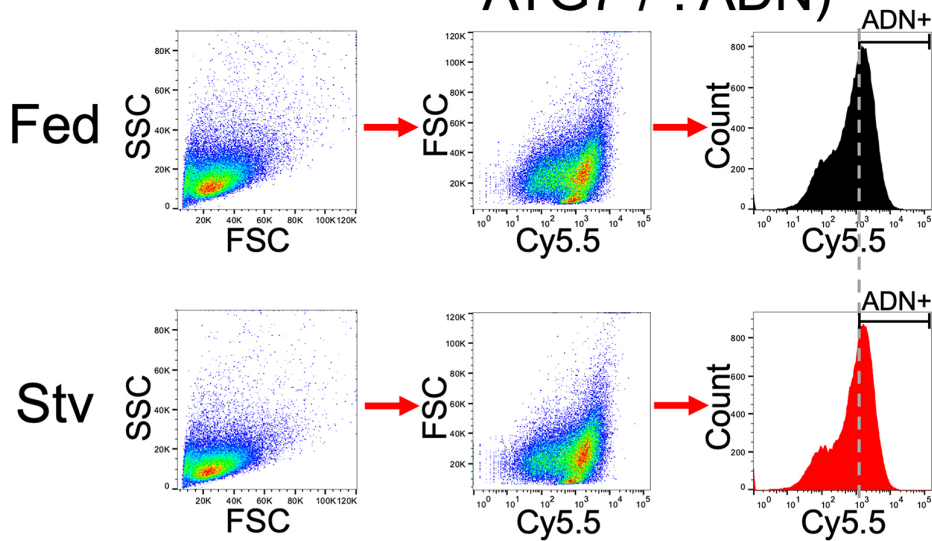

FACS gating strategy used in Figure 2C-D. Scatter plots and histograms with the gating strategy used are shown. Applies to Figure 2C and Figure 2D.

Figure 2C-D (H9C2 cells Fed vs. Stv: FH-D-Iso)

FACs gating strategy used in Figure 2C-D. Scatter plots and histograms with the gating strategy used are shown. Applies to Figure 2C and Figure 2D.

Figure 2E (Murine Embryonic Fibroblast Wildtype: ADN)

FACs gating strategy used in Figure 2E. Scatter plots and histograms with the gating strategy used are shown.
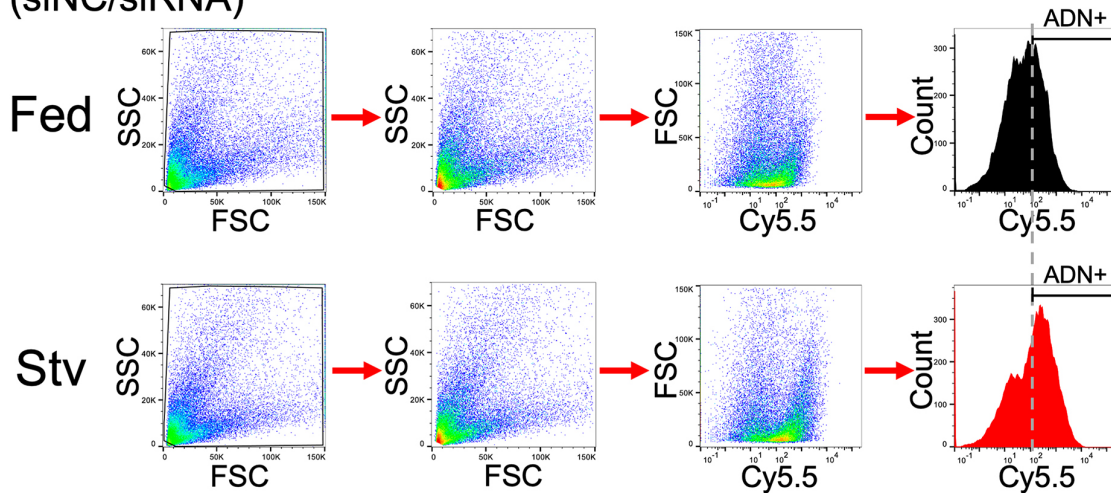

Figure 2F (Murine Embryonic Fibroblast ATG5-/-: ADN)

FACs gating strategy used in Figure 2F. Scatter plots and histograms with the gating strategy used are shown.

Figure 2G (Murine Embryonic Fibroblast ATG7-/-: ADN)

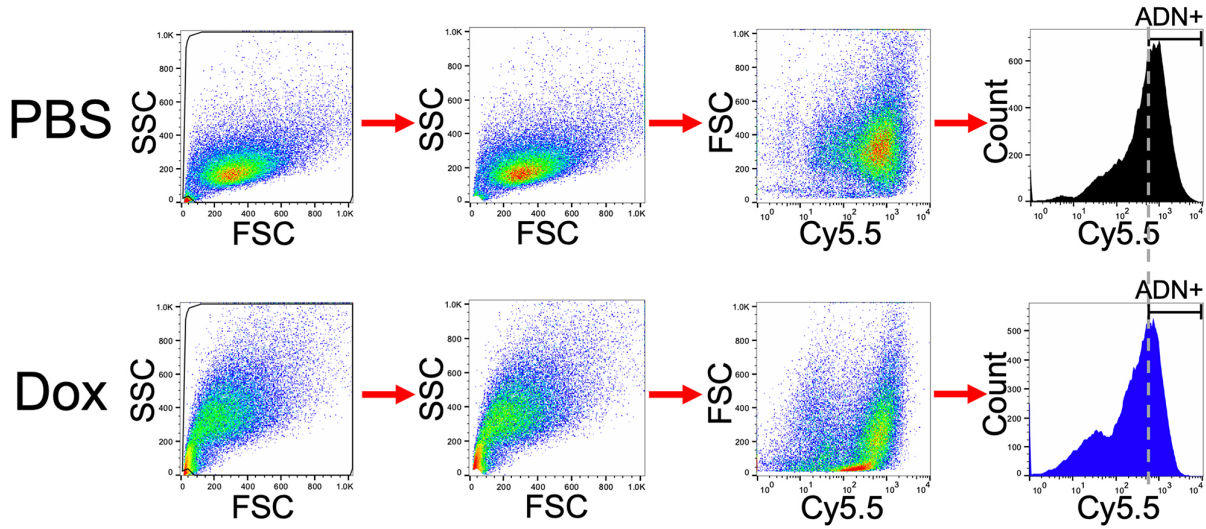FACs gating strategy used in Figure 2G. Scatter plots and histograms with the gating strategy used are shown.

Figure 2I (siNC/siRNA) (H9C2 cells ATG7 siRNA Fed vs. Stv: ADN)

FACs gating strategy used in Figure 2I. Scatter plots and histograms with the gating strategy used are shown.
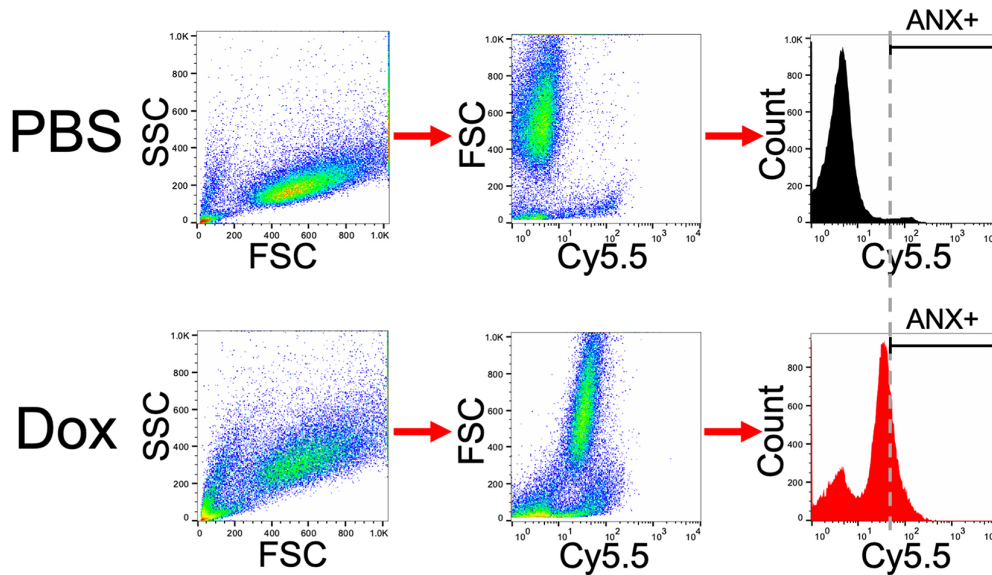
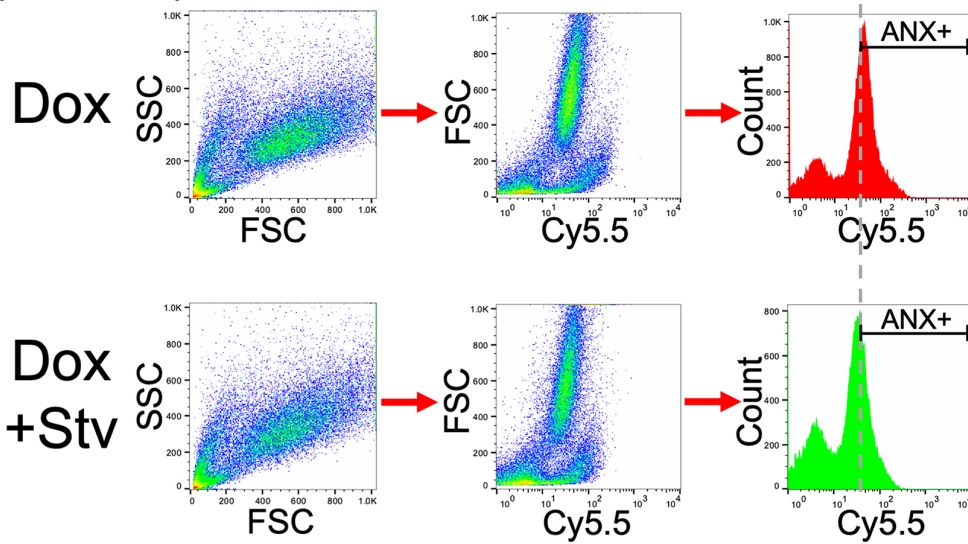# Figure 4E (H9C2 cells PBS vs. Dox: ADN)

FACs gating strategy used in Figure 4E. Scatter plots and histograms with the gating strategy used are shown.

Figure 4F (H9C2 cells PBS vs. Dox: ANX)

FACs gating strategy used in Figure 4F. Scatter plots and histograms with the gating strategy used are shown.

Figure 4J
(4H/4I/4J) (H9C2 cells Dox vs. Dox+Stv: ANX)

FACs gating strategy used in Figure 4J. Scatter plots and histograms with the gating strategy used are shown. Applies to Figure 4H, Figure 4I and Figure 4J.